

From point to extended defects in two-dimensional MoS₂: Evolution of atomic structure under electron irradiation

Hannu-Pekka Komsa,¹ Simon Kurasch,² Ossi Lehtinen,² Ute Kaiser,² and Arkady V. Krasheninnikov^{1,3}

¹*Department of Physics, University of Helsinki, P.O. Box 43, 00014 Helsinki, Finland*

²*Central Facility for Electron Microscopy, Group of Electron Microscopy of Materials Science, University of Ulm, 89081 Ulm, Germany*

³*Department of Applied Physics, Aalto University, P.O. Box 11100, 00076 Aalto, Finland*

(Received 12 April 2013; revised manuscript received 19 June 2013; published 2 July 2013)

By combining high-resolution transmission electron microscopy experiments and first-principles calculations, we study production, diffusion, and agglomeration of sulfur vacancies in monolayer MoS₂ under electron irradiation. Single vacancies are found to be mobile under the electron beam and tend to agglomerate into lines. Different kinds of such extended defects are identified in the experiments, and their atomic structures and electronic properties are determined with the help of calculations. The orientation of line defects is found to be sensitive to mechanical strain. Our calculations also indicate that the electronic properties of the extended defects can be tuned by filling vacancy lines with other atomic species, thereby suggesting a way for strain and electron-beam-assisted engineering of MoS₂-based nanostructures.

DOI: [10.1103/PhysRevB.88.035301](https://doi.org/10.1103/PhysRevB.88.035301)

PACS number(s): 61.80.Fe, 61.72.Cc, 68.37.Og, 31.15.es

I. INTRODUCTION

Inorganic two-dimensional (2D) transition metal dichalcogenide (TMD) monolayers have recently been manufactured by mechanical^{1,2} and chemical^{3,4} exfoliation of their layered bulk counterparts, as well as by chemical vapor deposition.^{5–7} The TMDs have a common structural formula MX₂, where M stands for transition metals (Mo, W, Ti, etc.) and X for chalcogens (S, Se, Te).^{8,9} The prototypical TMD material is MoS₂,^{10,11} which is a semiconductor with an optical band gap of about 2 eV.^{12,13} It can be doped *n* or *p* type,¹⁴ and shows fairly high carrier mobilities,² excellent mechanical characteristics,¹⁵ and intriguing optical properties.^{16,17} These properties may find use in logical devices,^{2,18} flexible electronics,^{15,19} photonics,^{20,21} and gas sensing.^{22,23}

High-resolution transmission electron microscopy (HR-TEM) has been used in numerous studies to characterize 2D materials with atomic resolution. This technique has also been applied to various TMDs.^{4,6,7,24,25} It is well known that exposure to the electron beam during imaging can lead to production of defects in the sample, either due to ballistic displacement of atoms,^{26–28} beam-stimulated chemical etching,²⁹ or ionization damage.³⁰ All these mechanisms can be active in flat^{31–34} and rolled-up TMD sheets³⁵ depending on electron voltage, vacuum level, beam current, and sample morphology.

It has also been found that prolonged electron irradiation may give rise to the development of new morphologies in a 2D sample, such as triangular holes in BN,^{36,37} amorphous networks,³⁸ “flower” defects,^{39,40} and dislocations^{41,42} in graphene. Moreover, postsynthesis substitutional doping of BN sheets has been shown⁴³ using *in situ* electron-beam irradiation inside a TEM, with the system being transformed from electrical insulator to conductor due to the substitution of boron with carbon atoms coming from the decomposition of hydrocarbon molecules under the beam. However, very little is known about the effects of prolonged irradiation on 2D TMDs, and in particular on the agglomeration of defects or beam-induced substitutional reactions.

In this work, using HR-TEM, we monitor *in situ* vacancy production and agglomeration under prolonged exposure to

the electron beam. As the vacancy concentration increases, the vacancies predominantly form extended line defects. With the help of first-principles simulations, we identify the probable atomic configuration of the lines. We also study the effects of strain on line defect formation. Finally, we discuss the substitution processes and the electronic structure of MoS₂ sheets with line defects.

II. METHODS

Free standing monolayer MoS₂ samples (note that the monolayer consists of three atomic layers) were prepared by mechanical exfoliation of natural MoS₂ bulk crystals, followed by characterization via optical microscopy on a Si+90 nm SiO₂ substrate and transfer to a perforated TEM support film (Quantifoil), as described in Ref. 33. Aberration-corrected AC-HRTEM imaging was carried out at room temperature in an image-side Cs corrected FEI TITAN microscope operated at a primary beam energy of 80 keV, a current density of $\sim 1.3 \times 10^6$ e/nm²/s, and single frame acquisition time of 1 s. The contrast difference between the Mo and S sublattice is clearly detectable in the AC-HRTEM images proving the monolayer nature of the sheet (for a bilayer the contrast would be identical as Mo is stacked above S). This is also confirmed in diffraction measurements, as successive diffraction spots from one $\{hkl\}$ family show different intensity, whereas for bi- and multilayers, they are equal.²⁴ The analyzed intensity ratio of the $\{\bar{1}100\}$ diffraction spots was found to be 1.07.

Our first-principles calculations were carried out within the framework of the density-functional theory (DFT) implemented in the VASP package^{44,45} based on plane-wave basis and the projector augmented wave formalism.⁴⁶ Electron-electron interactions were treated using the Perdew-Burke-Ernzerhof (PBE) exchange-correlation functional.⁴⁷ As we here only consider defects within single layer MoS₂ sheets, PBE is expected to provide good description of the local properties, without the need for dispersion-corrected (van der Waals) functionals. In order to accommodate the long-range strain fields of the defect structures within the computational cell,

we use a relatively large rectangular $10 \times 8\sqrt{3}$ supercell of MoS₂. Migration paths are calculated using the nudged elastic band (NEB) method.⁴⁸

The relative formation energy E_f of vacancy agglomerates is given with respect to the same number N_{vac} of isolated vacancies:

$$E_f(N_{\text{vac}}) = E_{\text{tot}}(N_{\text{vac}}) - N_{\text{vac}}E_{\text{tot}}(\text{SV}), \quad (1)$$

where $E_{\text{tot}}(N_{\text{vac}})$ and $E_{\text{tot}}(\text{SV})$ are the total energy of supercells containing N_{vac} vacancies and a single vacancy, respectively. The relative formation energy of an isolated vacancy is then zero by definition. Negative values of E_f point towards the tendency of vacancies to agglomerate, while positive values indicate that such configurations are energetically unfavorable.

III. RESULTS

A. Line formation under electron irradiation in a TEM

The initial AC-HRTEM image of the sample is shown in Fig. 1(a). It contains a number of vacancies, which may have already appeared due to the TEM-grid transfer procedure. On the other hand, vacancies and substitutional impurities could have been present in the starting material (with any light elements rapidly sputtered from the sample). During imaging, new vacancies are continuously produced, as was already reported in Ref. 33. The vacancies are also seen to diffuse, although at a fairly slow rate, to be discussed in more detail in Sec. III C.

With increasing vacancy concentration, defect agglomeration is expected. Here, formation of extended line defects is observed instead of, e.g., triangular vacancy clusters. The atomic structure of these lines appear to be well described by a row of single vacancies [cf. SV in Fig. 1(d)], without significant atomic reconstruction. However, the tendency to line up and to remain as a line is not very strong, suggesting that the energy gain is small.

After prolonged exposure to the electron beam, and further increase in vacancy concentration, the nature of the lines changes. The lines become wider, where, in essence, the lines extend to span two neighboring rows of the S sublattice. Figures 1(b) and 1(c) show two sequential images of the formation of this kind of vacancy lines. During the formation, the number of single vacancies surrounding the line has dropped significantly, suggesting that the line is formed through agglomeration of these vacancies rather than through production of a large number of new vacancies. The positions of the vacancies far from the line defect remain the same. Furthermore, the atomic structure has undergone significant changes as compared to the single vacancy line.

B. Determination of the atomic structure of line defects

Representative experimental images of the two types of vacancy lines, from here on denoted as single vacancy (SV) and double vacancy (DV) lines, are shown in Figs. 2(a) and 2(d). In order to determine the underlying atomic structure, we performed first-principles calculations for various atomic models corresponding to vacancy lines. The optimized geometries [shown in Figs. 2(b), 2(e), 2(g), and 2(i)—note that the bottom views are given in panels (b), (e), (g), and (i)] are used as

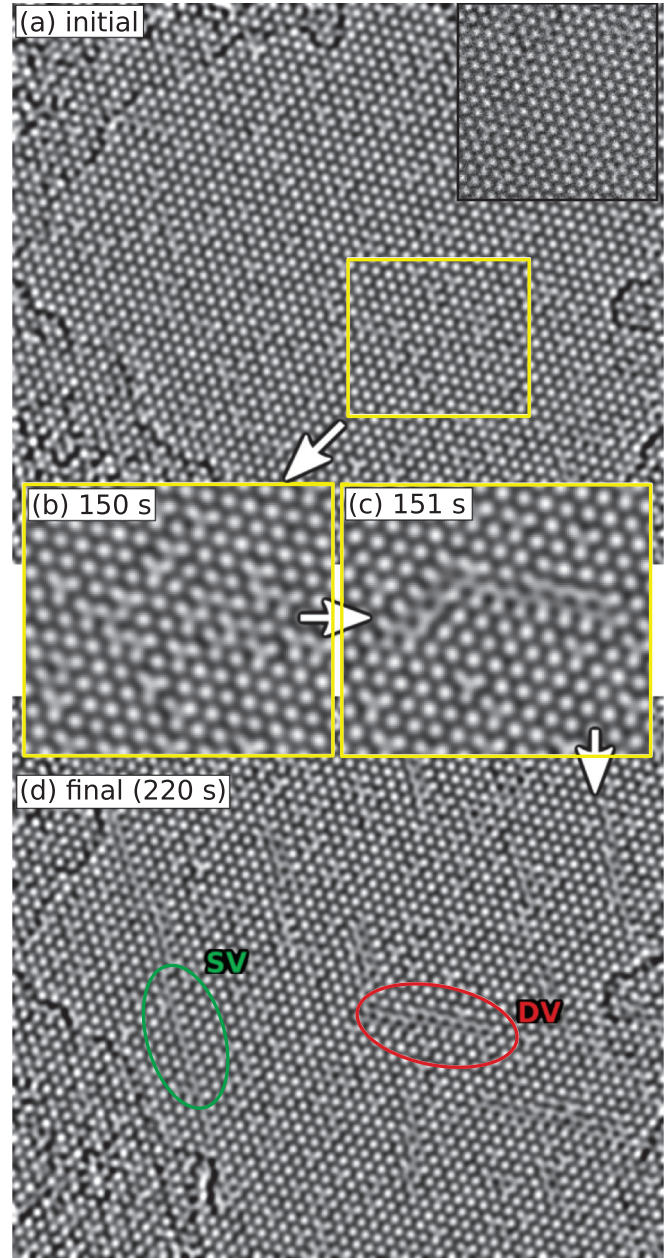


FIG. 1. (Color online) HR-TEM images showing the formation of line defects under electron irradiation at 80 kV. (a) The initial configuration with a certain number of S vacancies already present. (b) and (c) Intermediate configurations illustrating formation of defect lines through agglomeration of nearby vacancies. (d) The final configuration after 220 s, where a large number of defect lines can be seen. Examples of single vacancy (SV) and double vacancy (DV) lines are highlighted. The shape of the DV line has changed from that shown in (c). The HR-TEM frames are low pass filtered in order to reduce Poisson noise. An unprocessed region is shown in the upper-right corner of (a).

an input for TEM image simulation [see Figs. 2(c), 2(f), 2(h), and 2(j)], which are then compared to the experimental images. The images were simulated using Cs of 0.02 mm and the corresponding Scherzer focus of -11.2 nm. The relative formation energies for these structures are given in Fig. 2(k).

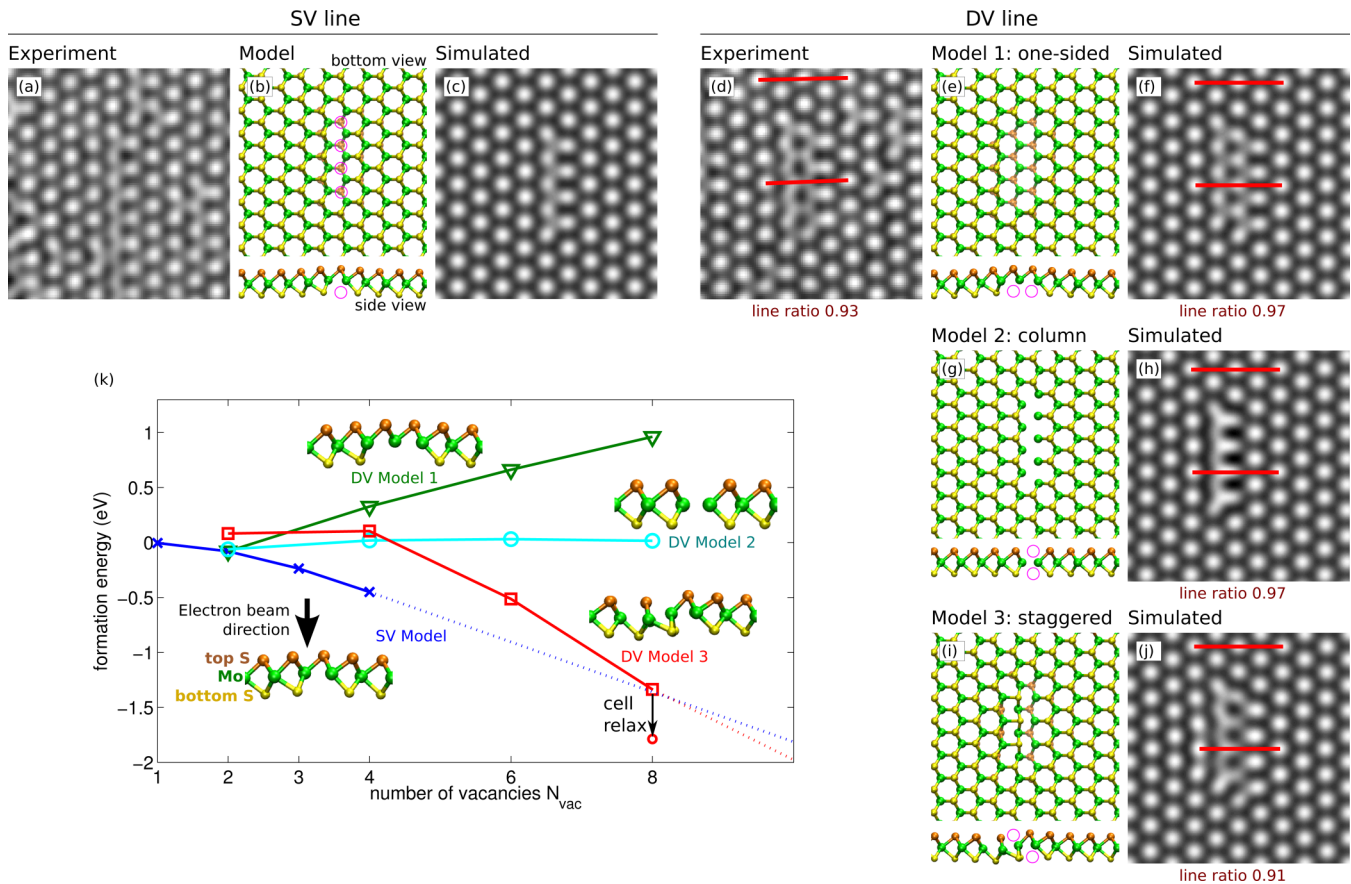


FIG. 2. (Color online) Comparison of experimental and simulated TEM images. (a,d) Examples of experimental HR-TEM images of the SV and DV lines with filtering applied as in Fig. 1. Various models of the vacancy lines: (b) and (c) single vacancy line, (e) and (f) two neighboring vacancy lines in the same S layer, (g) and (h) two vacancy lines coinciding in top and bottom layers, and (i) and (j) two vacancy lines in staggered configuration. The atomic structures (b), (e), (g), and (i) are obtained from DFT calculations and used to simulate TEM images (c), (f), (h), and (j). Note that the bottom and side views are shown. In order to differentiate between atoms in the two S layers, they are colored differently: orange for the top layer and yellow for the bottom layer. Magenta circles denote the initial vacancy positions. For DV lines, the local shrinkage of the lattice is quantified by a ratio of the length of line segments (solid red lines) in pristine lattice and around the defect. (k) Formation energies for all considered models as a function of the number of constituting single vacancies (the number of missing S atoms). The DV lines always have even number of vacancies. The extrapolation to longer lines is also shown. The insets are the side views of the atomic models presented in (b), (e), (g), and (i).

In the case of SV lines, there is only one reasonable choice for the underlying atomic structure, and the simulated and experimental images agree well. The formation energies show that agglomeration to a line leads to energy gain of about 0.05–0.2 eV per S vacancy, agreeing well with the tendency to line up.

A typical experimental image for a line of double vacancies (DV) is shown in Fig. 2(d). The structure has reconstructed, and several possible atomic structures can be envisioned. The three models attempted here are shown in Figs. 2(e), 2(g), and 2(i), and correspond to (1) two neighboring lines of S vacancies at the same side of the MoS₂. (2) Two lines of vacancies at the opposite sides of the MoS₂ thereby forming a line of vacancy columns (subsequently showing Mo-Mo bonds with bond length close to that in bulk Mo). (3) Two lines of vacancies are at the neighboring sites and opposite sides in “staggered” configuration. From the comparison of the simulated and experimental TEM images, it is clear that the agreement is good only for the staggered model. In addition

to the general features of the images, we also found agreement in the lattice contraction perpendicular to the line, as indicated by the ratios of line segments (the red lines in Fig. 2). Furthermore, the only model yielding negative formation energies is the staggered one. Equal number of vacancies on both sides of the monolayer leads to minimal bending of the sample and thereby promotes lower formation energies. When the length of the line exceeds four units ($N_{vac} > 8$), this kind of vacancy lines become energetically favored over the SV lines. Therefore the DV line in experiments is assigned to this structure (model 3).

For all the line structures discussed above, vacancies along the line were always on the same side of the monolayer. This is due to the fact that the formation energies tend to increase whenever the vacancies are on different sides of the sheet, but in the same line. For example, the formation energy of an SV line of length 4 with all vacancies on the same side showed 0.7 eV lower formation energy as compared to a case with the vacancies placed in an up-down-up-down configuration. We

stress that vacancy formation should occur predominantly on the bottom layer, but it is not possible to distinguish between top and bottom S vacancies in our AC-HRTEM setup.

We note that the atomic structures of these lines are different from those found in Refs. 49 and 50. Whereas our lines are produced by the electron irradiation in a pristine lattice, the lines in Refs. 49 and 50 were related to grain boundaries occurring during the growth. Interestingly, in Ref. 51, continuing irradiation was found to lead to extremely thin nanowires of Mo_5S_4 stoichiometry. Similar wires were also observed in our experiments.

C. Vacancy dynamics

The rate of identifiable single vacancy diffusion events in our experiments is fairly small. In order to estimate the rate, we counted the number of jumps before the start of line formation and obtained on average 0.023 jumps per second per vacancy (translating to a diffusion coefficient of $3.8 \times 10^{-18} \text{ cm}^2/\text{s}$). The events are clearly distinguishable during imaging, where single image capture takes about 1 s. Examples of diffusion events are shown in Figs. 3(a)–3(d). In the panel (a), a vacancy is created presumably in the bottom S layer. This and another vacancy are seen to diffuse in panels (b)–(d), whereas other vacancies remain fixed. Indeed, during the experiments, some vacancies appeared much more mobile, whereas others remained mostly fixed during the whole imaging period.

We stress that the diffusion is likely caused by the impacts of energetic electrons, as discussed below. It is expected that for S in the top layer, the diffusion has very low probability since the transferred momentum is always downwards. The mobile and immobile vacancies can then be assigned to vacancies in the bottom and top layers, respectively.

This is also supported by the calculated migration barrier of 2.3 eV, shown in Fig. 3. This barrier is too high for significant diffusion at room temperature under thermal equilibrium. However, the sample is under continuous bombardment by energetic electrons. In order to check whether diffusion events could occur under the electron beam, we assign to a sulfur atom (one of the nearest neighbors to the vacancy) at the bottom layer kinetic energy corresponding to the amount of energy transferred to the recoil atom by a high-energy electron in a binary collision, and carry out molecular dynamics (MD) simulations to find out whether diffusion event occurs. A successful reproduction of diffusion events in our MD simulations required electron energy of 95 keV. This is very close to the threshold electron energy for vacancy creation found previously.³³ Although this value is slightly higher than 80 keV used in the experiments, a nonzero probability for these events is expected when the ionic movement at finite temperatures is accounted for in the cross-section calculation.²⁶

The SV lines are found to form fairly slowly, and often via diffusion of single vacancies. In contrast, the formation of the DV line was usually rapid, often occurring within a time interval of one frame. Therefore the isolated steps leading to the line defect could not be resolved. However, as the line was formed, the nearby vacancies were removed [cf. Figs. 1(b) and 1(c)], suggesting that the vacancies agglomerated. This is not consistent with the simple picture of slow vacancy

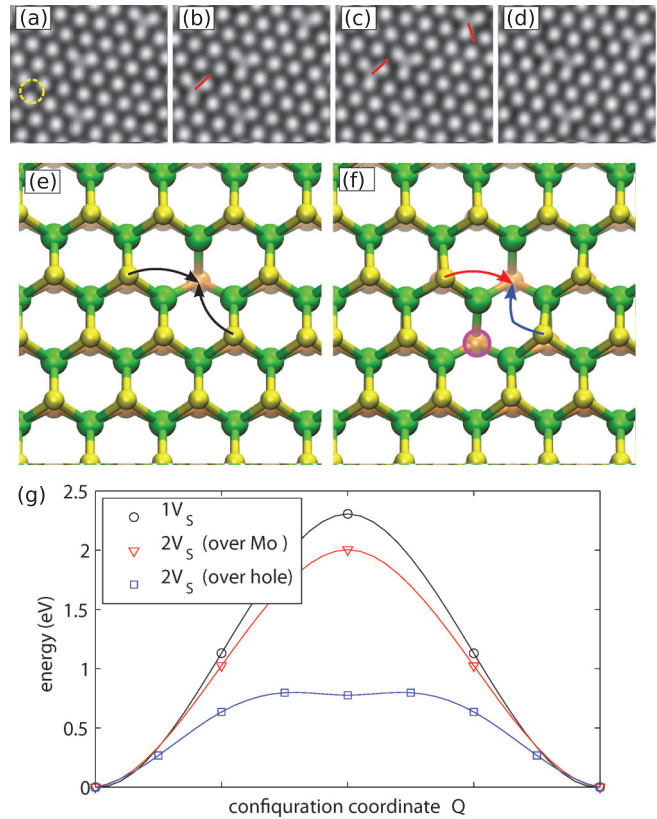


FIG. 3. (Color online) (a) Four sequential AC-HRTEM images showing vacancy diffusion events (highlighted by red line segments). (e) and (f) Calculated diffusion paths in the cases of (e) diffusion of S atom to a nearest-neighbor single vacancy site, (f) diffusion of S atom to a vacancy site in the presence of another nearby vacancy on the same side of the layer [position shown with a circle (magenta)]. In this case, there are two inequivalent paths. The respective energy barriers are given in (g).

diffusion rate discussed above. However, our calculations also suggest that the migration barrier is dramatically lowered, and thereby the diffusion rate is enhanced, when the number of vacancies in the nearby S sites (on the same side) is increased. Figure 3 also shows the calculated barriers when additional S is removed adjacent to the diffusion path (in the two inequivalent cases). This can lower the barrier down to 0.8 eV, which makes the diffusion under 80 kV electron beam significantly faster, and even makes thermal diffusion possible. We thus propose that, as the local vacancy concentration increases, the diffusion barrier may drop considerably and thereby accelerate the drive to the lowest-energy configuration.

During the formation of a DV line, as it contains vacancies on both sides of the monolayer, the transfer of S between top and bottom layers should play an important role. We could not observe this transfer directly. However, the calculated barrier for migration between top and bottom layers was found to be 3 eV and displacement threshold around 8.5 eV (110 kV electron energy). The values are slightly larger than for S sputtering or for single vacancy diffusion, but this process cannot be completely ruled out, especially when there are other vacancies in the nearby sites. During the continuous generation of new vacancies, the structures of these defect

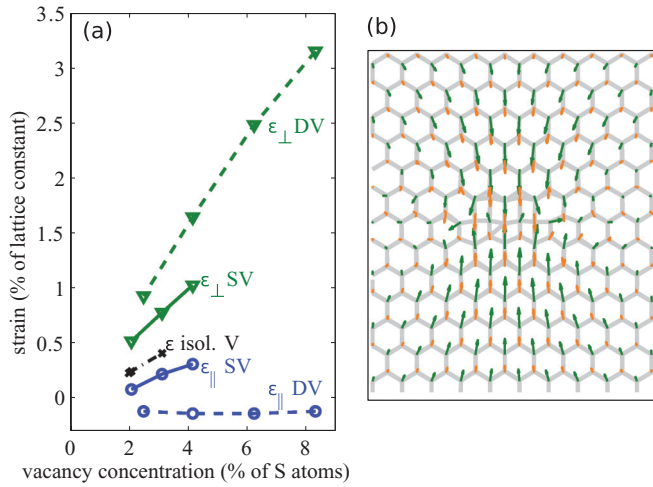


FIG. 4. (Color online) Lattice strain (shrinkage) as a function of vacancy concentration. The strain is isotropic in the case of isolated vacancies, but strongly anisotropic for vacancy lines. Strains in the direction parallel and perpendicular to the line are denoted by ϵ_{\parallel} and ϵ_{\perp} , respectively. (b) Strain field for DV line defect. The arrows denote atom displacement from its original position in a pristine lattice to its position in a defective lattice. The arrow length is artificially increased for visualization purposes.

lines also evolve in time. Not only do they grow, but also migrate occasionally. An example of DV line migration is seen in Figs. 1(c) and 1(d).

D. The effects of strain on vacancy agglomeration

The strong local lattice contraction around DV lines is evident from Figs. 2(d) and 2(j). Naturally, increasing vacancy concentration leads to contraction of the whole lattice. Figure 4(a) shows the calculated change in the supercell size (in terms of lattice constant) in the directions parallel and perpendicular to the SV and DV line as a function of vacancy concentration. These changes are obtained by minimizing the total energy of the defective system with respect to the supercell size. The case of isolated single vacancies is also shown for comparison. Single vacancies lead to isotropic contraction, while SV lines to slightly anisotropic contraction. In the case of DV lines, the size of the supercell perpendicular to the line ϵ_{\perp} contracts strongly, whereas the size parallel to the line ϵ_{\parallel} remains close to that of the pristine system. This can also be understood from the strain field of the DV line defect, which is visualized in Fig. 4(b), where arrows denote the atom displacement upon creation of the line. Displacements, and thereby the strain field, extend faraway in the direction perpendicular to the line defect, but affect very little the lattice outside the two end points.

On the other hand, the dependence of the formation energy of line defects on strain shown in Fig. 4 also means that external control of strain in the sample can favor formation of lines of particular orientation. In order to study this, we examined line formation at the freestanding edge of monolayer MoS₂. Figure 5(a) shows an HR-TEM image taken in the vicinity of the flake edge. On other sides, MoS₂ is clamped to the TEM grid. Initially, the edge is straight. After prolonged electron irradiation, the edge is bent inwards. Due to the instability

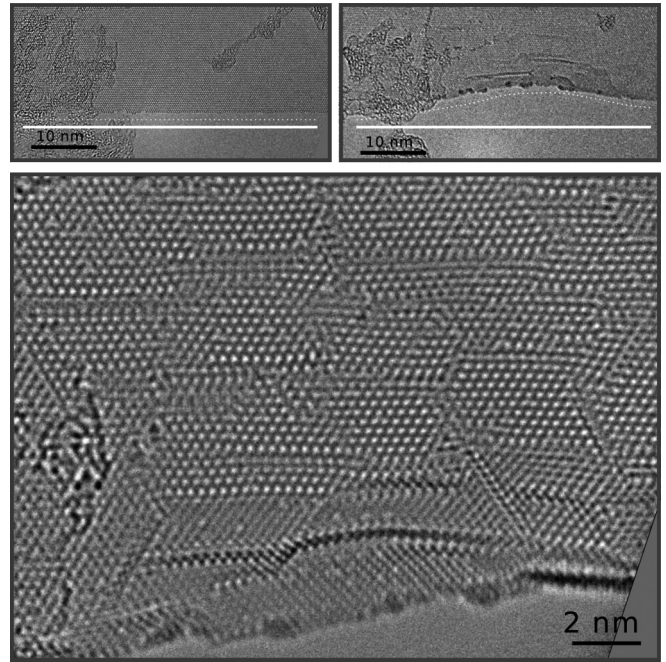


FIG. 5. AC-HRTEM images of the MoS₂ flake edge: (a) the initial configuration and (b) after 818 s of irradiation. The white horizontal lines are guides to the eye. (c) Magnification of the final configuration showing large concentration of lines, predominantly oriented parallel to the edge.

of the free-standing edge, the resolution at the edge is worse than in the rest of the sample. Most interesting, the majority of the line defects are seen to be directed parallel to the edge. This is enabled by the fact that stress can be released from the direction of the edge, but not from the perpendicular direction.

We propose that the full process leading to preferentially aligned line defects is the following [illustrated in Fig. 6]. (i) With increasing concentration of single vacancies, the lattice may release the stress from the direction of flake edges leaving the sample effectively under tensile strain from lateral directions. (ii) Such nonuniform strain favors formation of lines oriented parallel to edges by more than 50 meV per S vacancy. (iii) Formation of DV lines leads to additional contraction of the lattice perpendicular to the lines, but relieves the stress parallel to the line. Thus, active control of strain during electron irradiation should lead to formation of parallel lines.

For a sample that is clamped at all sides, the formation of line in one direction leads to perpendicular tensile stress, which makes it unfavorable to form further lines parallel to it.

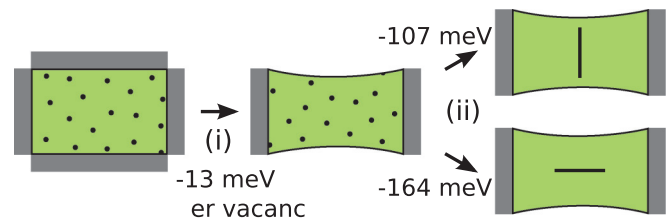


FIG. 6. (Color online) A sketch illustrating the formation and energetics of vacancy lines near the MoS₂ flake edge with referential orientation. The energies are normalized to the number of isolated vacancies, and calculated at the 3.1% vacancy concentration.

Consequently, the irradiation should lead to an equal number of lines with different orientations. Both cases have been seen in our experiments, depending on the clamping of the sample.

E. Line properties and substitution energetics

The lines observed in our experiments, and in particular, their directionality, could prove useful in various applications, which we will discuss next. Many material properties are expected to change as directional defects are introduced. For instance, optical response will depend on the polarization of light and catalytic activity may be enhanced for larger vacancy clusters.^{52,53} Here, we will limit our study on the electrical and magnetic properties of the lines.

It is worth mentioning first, that in addition to electron irradiation, isolated vacancies have been produced by voltage pulsing under the scanning tunneling microscope (STM).^{54–56} It was also later suggested that vacancy lines could be formed by STM, with calculations showing clearly increased conductance along the lines.⁵⁷ Such method provides more control than irradiation, although these methods are not easily scalable.

In the case of single vacancy, there is an unoccupied level in the upper half of the gap and an occupied level nearly degenerate with valence band maximum (VBM).^{33,58} The density of states of the SV and DV lines is shown in Figs. 7(b) and 7(d). In the case of SV line, the DOS is similar to that found in Ref. 57. The unoccupied levels widen to a band covering large portion of the band gap. The occupied vacancy levels do not interact strongly, and the system still retains a gap of about 0.5 eV. In practice, due to the existence of other defects in the system and possible effects of the environment, the Fermi level may lie within the defect band and thereby lead to enhanced conductivity parallel to the lines. In the case of the DV line,

the defect band widens further and the band gap closes, thus making the lines truly metallic.

Lines of naked vacancies are likely of very limited practical use due to their reactivity. However, the vacancy lines may be filled, and consequently functionalized, by other atoms as we reported for isolated vacancies.³³ When the sample is removed from the TEM chamber, the vacancies should get filled immediately with elements abundant in air such as N, O, and C. Our calculations indicate that, even in the case of fairly strongly reconstructed DV lines, filling of vacancy lines should lead to the same local geometry as if the substitution was carried out one vacancy at a time in pristine MoS₂. The density of states for various donor, acceptor, and isoelectronic substitutions to SV and DV lines is shown in Figs. 7(b) and 7(d) with the corresponding substitution energies given in Figs. 7(a) and 7(c). The substitution energy is defined as

$$E_{\text{sub}} = E_{\text{tot}}(X@Vac) - [E_{\text{tot}}(Vac) + \mu_X], \quad (2)$$

where $E_{\text{tot}}(X@Vac)$ and $E_{\text{tot}}(Vac)$ are the total energies of the supercells with species X inserted into the vacancy and with the bare vacancy, respectively. For the chemical potential of the substituting species μ_X , we consider three different references: isolated atoms, dimers, and molecules with hydrogen. The calculations are carried out for infinitely long vacancy lines and the energies are always given per vacancy.

Many of the substitution processes are energetically favorable, depending on the chemical environment. The energies tend to be slightly higher in the case of DV substitution, due to the low total energy of the DV vacancy lines. Therefore, in some cases, the single atom substitution energies given in Ref. 33 may better quantify the stability. O and Se are isoelectronic to S and lead to only minor changes in the electronic structure with respect to pristine MoS₂, thus effectively passivating the lines. Although it was previously found that S and Se like to form a random substitutional alloy

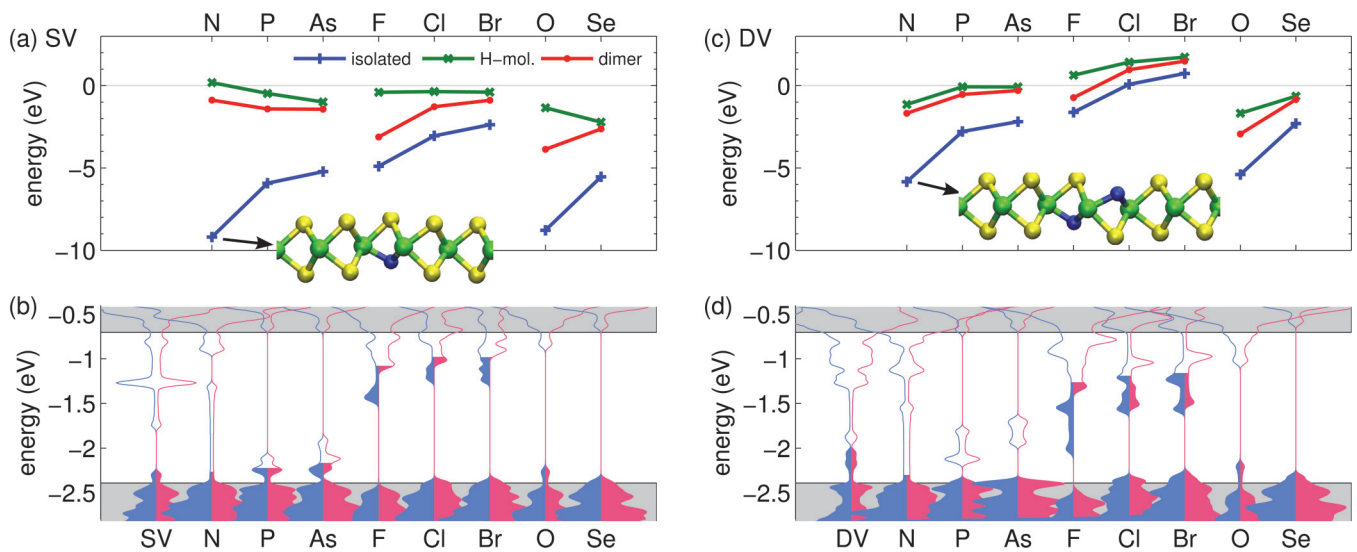


FIG. 7. (Color online) Energy (per atom) for foreign species substituting S atoms in SV (a) and DV (c) vacancy lines. Several references are used for the energy of the substituting atom: isolated atom (pluses, blue), molecules with H (crosses, green), and dimer molecules (dots, red). Density of states (DOS) for SV (b) and DV (d) vacancy lines, and for lines filled with various substituting species. In each case, the two curves correspond to the two spin (up and down) components. The filled DOS denotes occupied states (filled up to Fermi level). Gray areas mark for the valence and conduction bands. Examples of the atomic structures are also shown in the case of N substituted to the SV or DV line.

under thermal equilibrium,^{34,59} the approach proposed here could be used to circumvent these limitations to engineer lines filled with Se (or Te).

More interesting substituting species are from groups V and VII, as they lead to acceptor and donor doping, respectively. For SV lines, P, As, F, Cl, and Br all lead to formation of defect bands with fairly small band widths, but still predominantly retaining their acceptor and donor characteristics found for filling of isolated vacancies.³³ Common to all these systems is that the substituting atom is more strongly bonded to the Mo atoms perpendicular to the line. This leads to smaller coupling parallel to the line and therefore to narrower defect bands. Nitrogen substitution leads to extremely wide defect band spanning almost the whole gap. This is caused by the strong bonding of N to Mo atoms parallel to the line, which allows coupling between the N atoms and thereby leads to strong dispersion of the impurity band. For DV line substitution, in many cases, the defect bands widen even further. The curious cases here are P and As, which show defect bands in the middle of the gap.

The density of states also often shows spin-polarization. This is the case for all donors studied here, but for acceptors only in the case of As in the SV line. Therefore the conductivity should show spin selectivity in addition to the direction selectivity. Overall, postsynthesis electron-beam-mediated doping can provide more control over the magnetic response of MoS₂, as compared to that observed in bulk MoS₂,⁶⁰ edges of MoS₂ flakes,⁶¹ and proton irradiated samples.⁶²

IV. CONCLUSIONS

Our AC-HRTEM experiments indicate that prolonged electron irradiation of monolayer MoS₂ gives rise to agglomeration of sulfur vacancies into line defects due to migration of the defects. Different kinds of such extended defects consisting of one or two rows of vacancies were found, and their atomic structures and electronic properties were determined with the help of first-principles calculations. The orientation of line defects is sensitive to mechanical strain, and thus the direction of the lines may be controlled by application of external strain. The line defects can be filled with various impurity species, suggesting a way to alter the electronic and magnetic properties of monolayer MoS₂ with line defects. Overall, our results suggest a way for strain and electron-beam-assisted engineering of MoS₂-based nanostructures.

ACKNOWLEDGMENTS

We acknowledge financial support by the Academy of Finland through projects 218545, 266924, and 263416, the University of Helsinki Funds, and the Finnish Cultural Foundation. SK, OL, and UK are grateful to the German Research Foundation (DFG) and the State Baden Wuerttemberg in the frame of the SALVE (Sub Angstrom Low-Voltage Electron Microscopy) project and to the DFG in the frame of the SFB-TRR21 “Control of Quantum Correlations in Tailored Matter” project. We also thank CSC Finland for generous grants of computer time.

-
- ¹K. S. Novoselov, D. Jiang, F. Schedin, T. J. Booth, V. V. Khotkevich, S. V. Morozov, and A. K. Geim, *Proc. Natl. Acad. Sci. USA* **102**, 10451 (2005).
- ²B. Radisavljevic, A. Radenovic, J. Brivio, V. Giacometti, and A. Kis, *Nat. Nanotechnology* **6**, 147 (2011).
- ³G. Eda, H. Yamaguchi, D. Voiry, T. Fujita, and M. Chen, *Nano Lett.* **11**, 5111 (2011).
- ⁴J. N. Coleman *et al.*, *Science* **331**, 568 (2011).
- ⁵K. Kim, A. Hsu, X. Jia, S. Kim, Y. Shi, M. Hofmann, D. Nezich, J. Rodriguez-Nieva, M. Dresselhaus, T. Palacios, and J. Kong, *Nano Lett.* **12**, 161 (2012).
- ⁶Y. Zhan, Z. Liu, S. Najmaei, P. M. Ajayan, and J. Lou, *Small* **8**, 966 (2012).
- ⁷Y. Shi, W. Zhou, A.-Y. Lu, W. Fang, Y.-H. Lee, A. L. Hsu, S. M. Kim, K. K. Kim, H. Y. Yang, L.-J. Li, J.-C. Idrobo, and J. Kong, *Nano Lett.* **12**, 2784 (2012).
- ⁸J. Wilson and A. Yoffe, *Adv. Phys.* **18**, 193 (1969).
- ⁹C. Ataca, H. Şahin, and S. Ciraci, *J. Phys. Chem. C* **116**, 8983 (2012).
- ¹⁰Y. Feldman, E. Wasserman, D. J. Srolovitz, and R. Tenne, *Science* **267**, 222 (1995).
- ¹¹Q. H. Wang, K. Kalantar-Zadeh, A. Kis, J. N. Coleman, and M. S. Strano, *Nat. Nanotechnology* **7**, 699 (2012).
- ¹²K. F. Mak, C. Lee, J. Hone, J. Shan, and T. F. Heinz, *Phys. Rev. Lett.* **105**, 136805 (2010).
- ¹³H.-P. Komsa and A. V. Krasheninnikov, *Phys. Rev. B* **86**, 241201 (2012).
- ¹⁴L. Yadgarov, R. Rosentsveig, G. Leitus, A. Albu-Yaron, A. Moshkovich, V. Perflyev, R. Vasic, A. I. Frenkel, A. N. Enyashin, G. Seifert, L. Rapoport, and R. Tenne, *Angew. Chem., Int. Ed.* **51**, 1148 (2012).
- ¹⁵S. Bertolazzi, J. Brivio, and A. Kis, *ACS Nano* **5**, 9703 (2011).
- ¹⁶H. Zeng, J. Dai, W. Yao, D. Xiao, and X. Cui, *Nat. Nanotechnology* **7**, 490 (2012).
- ¹⁷K. F. Mak, K. He, J. Shan, and T. F. Heinz, *Nat. Nanotechnology* **7**, 494 (2012).
- ¹⁸H. Wang, L. Yu, Y.-H. Lee, Y. Shi, A. Hsu, M. L. Chin, L.-J. Li, M. Dubey, J. Kong, and T. Palacios, *Nano Lett.* **12**, 4674 (2012).
- ¹⁹J. Pu, Y. Yomogida, K.-K. Liu, L.-J. Li, Y. Iwasa, and T. Takenobu, *Nano Lett.* **12**, 4013 (2012).
- ²⁰Z. Yin, H. Li, H. Li, L. Jiang, Y. Shi, Y. Sun, G. Lu, Q. Zhang, X. Chen, and H. Zhang, *ACS Nano* **6**, 74 (2012).
- ²¹H. R. Gutiérrez, N. Perea-López, A. L. Elías, A. Berkdemir, B. Wang, R. Lv, F. López-Urías, V. H. Crespi, H. Terrones, and M. Terrones, *Nano Lett.* (2013), doi: 10.1021/nl3026357.
- ²²H. Li, Z. Yin, Q. He, H. Li, X. Huang, G. Lu, D. W. H. Fam, A. I. Y. Tok, Q. Zhang, and H. Zhang, *Small* **8**, 63 (2012).
- ²³F. K. Perkins, A. L. Friedman, E. Cobas, P. M. Campbell, G. G. Jernigan, and B. T. Jonker, *Nano Lett.* **13**, 668 (2013).
- ²⁴J. Brivio, D. T. L. Alexander, and A. Kis, *Nano Lett.* **11**, 5148 (2011).
- ²⁵G. Eda, T. Fujita, H. Yamaguchi, D. Voiry, M. Chen, and M. Chhowalla, *ACS Nano* **6**, 7311 (2012).

- ²⁶J. C. Meyer, F. Eder, S. Kurasch, V. Skakalova, J. Kotakoski, H. J. Park, S. Roth, A. Chuvilin, S. Eyhusen, G. Benner, A. V. Krasheninnikov, and U. Kaiser, *Phys. Rev. Lett.* **108**, 196102 (2012).
- ²⁷J. Kotakoski, C. H. Jin, O. Lehtinen, K. Suenaga, and A. V. Krasheninnikov, *Phys. Rev. B* **82**, 113404 (2010).
- ²⁸F. Banhart, *Rep. Prog. Phys.* **62**, 1181 (1999).
- ²⁹K. Mølhave, S. B. Gudnason, A. T. Pedersen, C. H. Clausen, A. Horsewell, and P. Bøggild, *Ultramicroscopy* **108**, 52 (2007).
- ³⁰R. F. Egerton, P. Li, and M. Malac, *Micron* **35**, 399 (2004).
- ³¹Z. Liu, K. Suenaga, Z. Wang, Z. Shi, E. Okunishi, and S. Iijima, *Nat. Commun.* **2**, 213 (2011).
- ³²L. P. Hansen, Q. M. Ramasse, C. Kisielowski, M. Brorson, E. Johnson, H. Topsøe, and S. Helveg, *Angew. Chem. Int. Ed.* **50**, 10153 (2011).
- ³³H.-P. Komsa, J. Kotakoski, S. Kurasch, O. Lehtinen, U. Kaiser, and A. V. Krasheninnikov, *Phys. Rev. Lett.* **109**, 035503 (2012).
- ³⁴D. O. Dumcenco, H. Kobayashi, Z. Liu, Y.-S. Huang, and K. Suenaga, *Nat. Commun.* **4**, 1351 (2013).
- ³⁵K. Ding, Y. Feng, S. Huang, B. Li, Y. Wang, H. Liu, and G. Qian, *Nanotechnology* **23**, 415703 (2012).
- ³⁶J. C. Meyer, A. Chuvilin, G. Algara-Siller, J. Biskupek, and U. Kaiser, *Nano Lett.* **9**, 2683 (2009).
- ³⁷C. Jin, F. Lin, K. Suenaga, and S. Iijima, *Phys. Rev. Lett.* **102**, 195505 (2009).
- ³⁸J. Kotakoski, A. V. Krasheninnikov, U. Kaiser, and J. C. Meyer, *Phys. Rev. Lett.* **106**, 105505 (2011).
- ³⁹S. Kurasch, J. Kotakoski, O. Lehtinen, V. Skákalová, J. Smet, C. E. Krill, A. V. Krasheninnikov, and U. Kaiser, *Nano Lett.* **12**, 3168 (2012).
- ⁴⁰A. W. Robertson, C. S. Allen, Y. a. Wu, K. He, J. Olivier, J. Neethling, A. I. Kirkland, and J. H. Warner, *Nat. Commun.* **3**, 1144 (2012).
- ⁴¹O. Lehtinen, S. Kurasch, A. V. Krasheninnikov, and U. Kaiser, *Nat. Commun.* **4**, 2098 (2013).
- ⁴²J. H. Warner, E. R. Margine, M. Mukai, A. W. Robertson, F. Giustino, and A. I. Kirkland, *Science* **337**, 209 (2012).
- ⁴³X. Wei, M. Wang, Y. Bando, and D. Golberg, *ACS Nano* **5**, 29162922 (2011).
- ⁴⁴G. Kresse and J. Hafner, *Phys. Rev. B* **47**, 558 (1993).
- ⁴⁵G. Kresse and J. Furthmüller, *Comput. Mater. Sci.* **6**, 15 (1996).
- ⁴⁶P. E. Blöchl, *Phys. Rev. B* **50**, 17953 (1994).
- ⁴⁷J. P. Perdew, K. Burke, and M. Ernzerhof, *Phys. Rev. Lett.* **77**, 3865 (1996).
- ⁴⁸G. Henkelman, B. P. Uberuaga, and H. Jónsson, *J. Chem. Phys.* **113**, 9901 (2000).
- ⁴⁹W. Zhou, X. Zou, S. Najmaei, Z. Liu, Y. Shi, J. Kong, J. Lou, P. M. Ajayan, B. I. Yakobson, and J.-C. Idrobo, *Nano Lett.* **13**, 2615 (2013).
- ⁵⁰A. N. Enyashin, M. Bar-Sadan, L. Houben, and G. Seifert, *J. Phys. Chem. C* **117**, 10842 (2013).
- ⁵¹X. Liu, T. Xu, X. Wu, Z. Zhang, J. Yu, H. Qiu, J.-H. Hong, C.-H. Jin, J.-X. Li, X.-R. Wang, L.-T. Sun, and W. Guo, *Nat. Commun.* **4**, 1776 (2013).
- ⁵²C. Ataca and S. Ciraci, *Phys. Rev. B* **85**, 195410 (2012).
- ⁵³S. Tongay, J. Zhou, C. Ataca, J. Liu, J. S. Kang, T. S. Matthews, L. You, J. Li, J. C. Grossman, and J. Wu, *Nano Lett.* **13**, 2831 (2013).
- ⁵⁴S. Hosoki, S. Hosaka, and T. Hasegawa, *Appl. Surf. Sci.* **60-61**, 643 (1992).
- ⁵⁵S. Hosaka, S. Hosoki, T. Hasegawa, H. Koyanagi, T. Shintani, and M. Miyamoto, *J. Vac. Sci. Technol. B* **13**, 2813 (1995).
- ⁵⁶J. D. Fuhr, A. Saúl, and J. O. Sofo, *Phys. Rev. Lett.* **92**, 026802 (2004).
- ⁵⁷K. S. Yong, D. M. Otalvaro, I. Duchemin, M. Saeys, and C. Joachim, *Phys. Rev. B* **77**, 205429 (2008).
- ⁵⁸C. Ataca and S. Ciraci, *J. Phys. Chem. C* **115**, 13303 (2011).
- ⁵⁹H.-P. Komsa and A. V. Krasheninnikov, *J. Phys. Chem. Lett.* **3**, 3652 (2012).
- ⁶⁰S. Tongay, S. S. Varnoosfaderani, B. R. Appleton, J. Wu, and A. F. Hebard, *Appl. Phys. Lett.* **101**, 123105 (2012).
- ⁶¹J. Zhang, J. M. Soon, K. P. Loh, J. Yin, J. Ding, M. B. Sullivan, and P. Wu, *Nano Lett.* **7**, 2370 (2007).
- ⁶²S. Mathew, K. Gopinadhan, T. K. Chan, X. J. Yu, D. Zhan, L. Cao, A. Rusydi, M. B. H. Breese, S. Dhar, Z. X. Shen, T. Venkatesan, and J. T. L. Thong, *Appl. Phys. Lett.* **101**, 102103 (2012).